Interrogation of a Precipitation Reaction by Electrical Resistance Tomography (ERT)

S. J. Stanley
Dept. of Chemical Engineering, UMIST, P.O. Box 88, Manchester, M60 1QD, U.K.

and

British Nuclear Fuels (BNFL), NSTS, Risley, Warrington, WA3 6AS, U.K.

R. Mann
Dept of Chemical Engineering, UMIST, P.O. Box 88, Manchester, M60 1QD, UK.

K. Primrose
Industrial Tomography Systems, 47 Newton Street, Manchester, M1 1FT, UK.

DOI 10.1002/aic.10359
Published online January 14, 2005 in Wiley InterScience (www.interscience.wiley.com).

Electrical resistance tomography (ERT) provides a noninvasive and nonintrusive technique for the full 3-D interrogation of a typical stirred vessel reactor up to a spatial discrimination of approximately 2,500 derived data points. Some recent ERT results are presented for a newly refurbished 8 ring 16-sensor 2.3 m^3 pilot scale vessel, detecting the conductivity changes throughout the whole volume of the vessel during the semi-batch precipitation of barium sulfate. Fast timewise acquisition at video frame rates provides an augmented-reality visualization of the precipitation process. Time evolving images created by solid-body iso-surfaces, which use color to denote conductivity, are presented during the proceeding reaction. These images provide a 5-D representation of the conductivity fields within the stirred vessel reactor. The conductivity (or pixel) distributions during the precipitation process provide a real-time measurement of the homogeneity within the vessel. The timewise conductivity profiles, over the whole of the vessel during the precipitation, indicate three very distinctive regions reflecting the complex reaction kinetics. The ERT system also highlights the very *different conductivity profiles during precipitation when the stirred vessel is operated without agitation. This application is believed to be the first example of ERT applied to a precipitation process. ERT offers new possibilities for control action linked to spatio-temporal distributions of phases and components for industrial applications.* © 2005 American Institute of Chemical Engineers *AIChE J,* 51: 607–614, 2005

Key words: precipitation, crystallization, barium sulfate, fluid mixing, stirred vessel, electrical resistance tomography (ERT).

Introduction

Crystallization is one of the oldest chemical engineering operations to have been exploited commercially. The crystallization of sparingly soluble substances, that is, crystallization by precipitation is rather poorly understood (Söhnel and Garside, 1992).[1] Precipitation is known to be extremely difficult to study due to the simultaneous and rapid occurrence of nucleation and growth coupled with the presence of secondary processes, such as ageing and agglomeration. The role of precipitation within industry is ever expanding, with additional applications in medicine, biology, and analytical chemistry. Stirred vessels are frequently encountered in the process indus-

tries, where they are often used as chemical reactors for the manufacture of the required solid precipitate. The interactions of fluid mixing are invariably complex and poorly understood, whether the mixing takes place in laminar, intermediate or turbulent flow regimes. This in itself poses a difficult problem, but when coupled with the complex kinetics encountered during any precipitation process, fully understanding the system appears almost impossible. Instrumentation to investigate mixing and chemical reaction (precipitation) is mostly very sparse or even nonexistent.

It is most desirable to be able to interrogate the full volume in 3-D inside a typical single feed semi-batch reactor. To map out the conductivity distribution in space would be most useful, as this provides a strong indication of the extent of mixing and/or reaction. If the spatial concentration fields could also be measured in 3-D, this would provide a powerful new basis for control of chemical reaction rates in space, which would offer the capability to suppress byproduct reactions by suitable control of concentration levels, their location and interaction. Electrical tomographic methods provide a means to obtain a 3-D scanning of the interior of the reactor space. The discrimination of spatial information can be as high as around 2,500 derived data points with fast acquisition.

The recent and rapid development of tomographic techniques, as applied to the process industries, can be judged by recent textbooks (Williams and Beck, 1995; Chaouki et al., 1997).[2,3] Electrical techniques developed and applied at UMIST, U.K., include electromagnetic (Yu et al, 1993),[4] capacitance (Dyakowski et al., 1999),[5] and resistance (Mann et al., 1997)[6] tomography. Earlier work has shown that an "8-level + 16-ring sensors" electrical resistance tomography (ERT) array could be applied at an industrial process vessel scale to measure salt concentration fields in 3-D during an unsteady tracer mixing test (Stanley et al., 2001).[7] Also, it was demonstrated that the pseudostationary distribution of gas holdup could be pictorialized in 3-D for typical stirred vessel gas-liquid mixing (Wang et al, 2000).[8] Subsequently, the UMIST/ITS ERT system was applied to demonstrate that the homogeneous single phase mixing created by different impeller types could be readily distinguished (Holden et al, 1998).[9] In addition, further work showed how such an ERT system could be use to diagnose the types of pathological mixing symptoms likely to be associated with equipment malfunction or failure (Holden *et al*., 1999).[10]

With up to around 2,500 derived data points within a stirred vessel, this density of measurements by ERT is ideal for validation of CFD calculations of just the fluid mixing (Sahu et al., 1999; Brucato et al., 2000),[11,12] or the especially complex situation when the fluid mixing is accompanied by reaction and solid formation in typical precipitation (Micale et al., 2000; Zauner et al., 2000).[13,14]

Most recently, it has become evident that ERT can be configured to measure the pseudostationary solids distribution inside a stirred vessel, as well as the solids distribution during the dynamic addition of a solids charge (Mann et al., 2001).[15] An application to the semibatch feed addition of strong brine (mimicking the semibatch addition of a feed reactant) has also been recently reported (Stanley et al., 2002).[16] The conductivity profile within the vessel during the semi-batch addition consisted of two main regions, reflecting the conductivity distribution during and after the semibatch feed time. ERT results for the semibatch addition of brine (that is, nonreactive) into the same stirred vessel were compared to

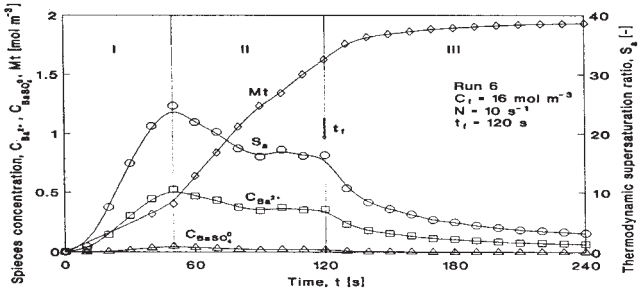

Figure 1. Typical variation of species concentration during $BaSO_4$ precipitation: Taguchi (1993) p. 152.

a fluid mixing model, namely the network-of-zones mixing model (Stanley et al., 2003).[17] The network-of zones model essentially splits the vessel interior into a number of descrete zones (12,000 for this particular simulation). A local mass balance is performed at each time increment for each of these individual zones or voxels which mimics the fluid mixing (Rahimi et al., 2001; Hristov, 2003).[18,19] Each of these examples suggests that ERT does provide a new means for direct experimental investigation of the rates of fluid mixing and reaction which accompany precipitation processes.

Earlier Precipitation Studies

Most previous investigations into barium sulfate precipitation have been concerned with the crystal size distribution (CSD) (Aoun et al., 1999; Phillips et al., 1999),[20,21] which can be influenced both by the intrinsic kinetics and the supersaturation levels. In order to define the influence of mixing it is, therefore, better to determine its separate influence on the supersaturation levels and kinetics.

Taguchi (1993)[22] investigated the influence of various operating variables on the timewise supersaturation profiles, and on the kinetics of nucleation and growth during the semibatch precipitation of barium sulfate in a small 150 mL jacketed glass precipitator. The supersaturation levels during the semi-batch operation were calculated from measured conductivity values (see Figure 1). The concentrations of free barium ions (C_{Ba}^{2+}), barium sulfate ion pairs, (C_{BaSO4}^{0}), magma density (M_t), and thermodynamic supersaturation ratio (S_a) were all calculated from a single conductivity probe measurement. The small vessel was taken to be perfectly mixed.

The concentration of free Barium ions C_{Ba}^{2+} was evaluated by the measurement of the overall conductivity of the solution. The thermodynamic supersaturation ratio of barium sulfate S_a, is given by

$$S_a = \frac{\gamma_{BaSO_4} C_{Ba}^{2+}}{\sqrt{K_{sp}^0}} \tag{1}$$

In reality, this supersaturation ratio (S_a) calculated by Taguchi represents a "bulk" supersaturation ratio, which only exists due to imperfect mixing. If the vessel was truly perfectly mixed, then the magnitude of the observed conductivities (and, therefore, conductivity derived supersaturation ratio) would be lower. This is because for this particular precipitating system the primary nucleation is very fast. When the two reactants do

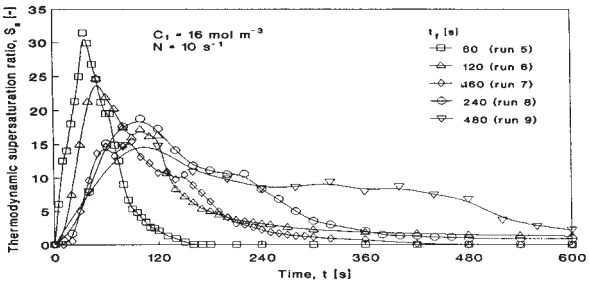

Figure 2. Supersaturation profiles for different feed times, t_f. Ref: Taguchi (1993) p. 153.

come into contact the supersaturation remains low due to the fast nucleation and growth as the particles form. The mean activity coefficient (as seen if Eq. 1) for barium sulfate γ_{BaSO4}, was calculated by the Debye-Huckel equation

$$-\log\gamma_{MA} = \frac{0.5091[Z_M\, Z_A]I^{1/2}}{1 + \kappa a} \tag{2}$$

In all the semi-batch experiments carried out by this researcher, the variations of these species concentrations showed three periods (see Figure 1). In the first period (I), C^2_{Ba} and C^0_{BaSO4} increased approximately monotonically with continued feeding of the reactant solution, until the primary nucleation of the precipitate is triggered by the rise in supersaturation S_a. The second period (II) lies between the time when the rate of increase of C^2_{Ba}, C^0_{BaSO4} begins to slow, and the time when the reactant feed ceases t_f. In this phase C^2_{Ba} and C^0_{BaSO4} decrease to reach a quasi-steady state, although the magma density M_t, increases significantly. In the last period (III) C^2_{Ba} and C^0_{BaSO4} decrease monotonically, while the magma density M_t increases slightly.

Of particular interest are the maximum levels of supersaturation obtained; the time at which peak supersaturation occurs; the supersaturation level at the end of the feed time t_f, and the rate of decrease of supersaturation in the last phase (III). These are all useful indicators of the rates of internal processes. Adjacent is a plot of thermodynamic supersaturation profiles for a set of different feed times ranging between 1 min and 8 min (see Figure 2).

It can be clearly seen that when the feed time t_f is small the peak supersaturation value is highest, and also occurs more quickly with a subsequent sharp fall in the supersaturation. For long feed times on the other hand, the peak supersaturation level is much lower, with the supersaturation then falling off much more slowly. In all cases the final supersaturation never falls to the starting supersaturation (zero).

Experimental Aim

The use of ERT to interrogate the single feed semi-batch precipitation of barium sulfate has been explored. The barium sulfate is formed by the following reaction

$$Na_2SO_4(aq) + BaCl_2(aq) \rightarrow 2NaCl(aq) + BaSO_4(s)\downarrow \tag{3}$$

The results are presented in a number of different ways. Time evolving conductivity profiles during the reaction are of strong interest as they should reflect the complex kinetics typical of all precipitation processes. These timewise conductivity profiles should incorporate both the effects caused by the semi-batch addition of the feed, as well as the formation of the barium sulfate solids (that is, mixing and reaction).

An augmented reality visualization during the feed addition phase of the precipitation process is achieved using solid-body iso-surfaces in conjunction with partially opaque see-through "pseudofluids" between the iso-surfaces. By careful grading of the degree of opacity from fully opaque to nonopaque, striking color images in 3-D can be reconstructed and assembled showing for example areas/colors with different concentrations or two-phase densities. These views can convey an understanding of the mixing behavior, which would otherwise be completely invisible or in contrast completely opaque (optically inaccessible). Also of particular interest are the conductivity frequency distributions over the whole volume of the vessel during the experiment, which provides a direct measurement of the conductivity distributions homogeneity.

Experimental Equipment

Each of the ERT experiments were carried out on a flat-bottomed polypropylene stirred tank of diameter T = 1.43 m, shown in Figure 3. The liquid height H inside the tank is equal to the tank diameter providing a total volume of around 2,300 litres (2.3 m^3). Each of the four full-length baffles of width T/10 are attached to the vessel wall by a number of polypropylene brackets. All experiments used the six-blade Rushton turbine of diameter D = T/3 = 0.477 m, which was set to a clearance of H/2 above the base. A variable speed motor providing speeds in the range of 75 to 250 rpm drives the impeller.

The electrical resistance tomography (ERT) system comprises of three components. The sensor electrodes/process vessel, the data acquisition system (DAS), and a user interface (see Figure 4). The process vessel is retrofitted with a newly designed ERT sensor array consisting of 16 vertical running sensor sections equally spaced around the vessel circumference as seen in Figure 5. The presence of these 16 vertical running sections creates an 8 plane sensor array, with each plane being equally spaced (16.5 cm apart) along the liquid height, H. Also in view is the semi-batch feedline, baffles, impeller, and im-

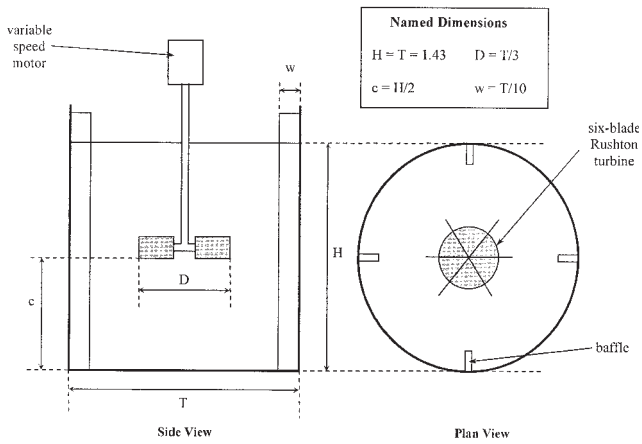

Figure 3. Stirred Vessel.

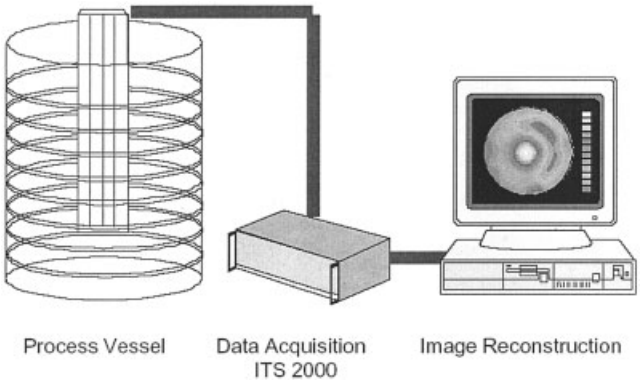

Figure 4. Electrical resistance tomography (ERT) system.

peller shaft. The sensors themselves comprise of simple stainless steel plates 100 mm x 38 mm. Each of the eight planes of electrode sensors communicates to the data acquisition system (DAS), via a network of co-axial cabling terminating with a 38-pin Centronic connector.

An ITS P2000 DAS (provided by Industrial Tomography Systems, Manchester, U.K.) was used to collect the required raw voltage measurements. The ITS P2000 DAS system was operated via a windows based software package (ITS System User 2000 v.4.0)[23]. The adjacent electrode protocol was employed to collect raw voltage measurements over each sensor electrode plane. This involves applying an AC current across an adjacent electrode pair and measuring the resultant potential difference across all the other possible adjacent electrode pairs. Once all measurements have been made, the AC drive current is "rotated" and applied to the next adjacent electrode pair and resultant voltage measurements are again taken. This process is repeated until all possible combinations have been exhausted (104 for a 16-sensor electrode plane). An image reconstruction algorithm (Linear Back Projection) is applied to convert these peripheral raw voltage measurements in to a 2-D conductivity map of the measurement area. Because the linear back projection (LBP) algorithm has a low computational requirement, the image reconstruction is performed online in real-time. Although, not applied here, an SCG iterative reconstruction algorithm is also available from Industrial Tomography Systems (Wang, 2002).[24]

The ERT system calibration technique involves taking a base line set of voltage measurements at a point in time, where the conductivity distribution inside the vessel is both homogeneous and known. The start of the experiment before any reactant has been added is usually a suitable reference condition. All other subsequent measurements can then be compared to the reference voltage measurements which enables the computation of each conductivity map (tomogram). The computed conductivity values are expressed as relative conductivity measurements. Care was taken to ensure that both the vessel contents and the reactant feed were at the same temperature.

The eight axial electrode planes, thus, give rise to $8 \times 104 = 832$ interrogative measures of the liquid volume (which in the case of $H = T$ is 2.3 m^3). The ERT systems resolution is often quoted roughly as around 5% of the vessel diameter (Holden et al., 1999),[10] although this does vary. It can depend on the nature of what we are trying to detect, that is, the magnitude of the conductivity variations, as well as the background conductivity. For example; a thin metallic rod smaller than 5% of the diameter will be detected while immersed in either tap water or brine; while a nonconducting rod of similar size will be detected while immersed in brine, but may not be detectable in tap water. The ease at which these theoretical "phantoms" are detected also varies with radial position. "Phantoms" closer to the wall are more easily detected as compared to "phantoms" in the center of the tank. Each reconstructed "tomogram" (image of the vessels cross-section at a particular sensor plane location) consists of a circular 20 pixel diameter image giving a total of some 316 spatial elements. Compared to the previously used Mk 1B-E (Holden et al., 1998)[9] system, the new ITS P2000 system has an improved temporal resolution providing up to 25 individual tomograms per s (that is, at video frame rates).

During the precipitation experiments a digital camera was employed to capture a view of the vessel at known times. All reactant feed solutions were prepared from analytical grade barium chloride, in the form of $BaCl_2.2H_2O$ hydrated crystals, (provided by Fisher, Ltd.) certified A.C.S. for purity. The anhydrous sodium sulfate was also provided by Fisher, Ltd.

Single Feed Semi-Batch Precipitation of Barium Sulfate

The eight-ring ERT system was used to monitor changes in the 3-D spatial conductivity field during the semi-batch precipitation of barium sulfate. Two experiments were conducted, the first with a semi-batch feed time t_f, of 7 min, the second with a shorter feed time of 4 min.

A number of issues, such as the size of the stirred vessel, as well as precipitate disposal meant that the concentrations of reactants and products were relatively low, with the total amount of barium sulfate formed being approximately 1kg for each feed time. The ERT system employed here would in fact be well suited to much higher reactant and product concentrations, although the injection current required by the system would have to be adjusted via the ITS software, to take into account the increase in conductivity of the reactant charge. In both cases, the feed reactant is the limiting component, that is, the feed determines the total amount of precipitate formed which was kept constant for both experiments. The precipitation process was initiated by adding exactly 40 dm^3, V_{feed}, of 0.1 M barium chloride feed solution over a known feed time t_f. This provides a volume to feed ratio V_{tank}/V_{feed}, of approxi-

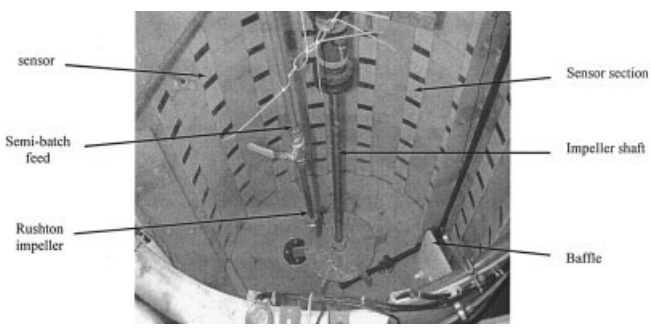

Figure 5. Refurbished eight plane, 16 electrode arrangement.

Table 1. Experimental Feed and Solute Concentrations

Chemical	Volume (dm^3)	Concentration (Mol l^{-1})	Quantity (Mol)	Quantity (g)
Barium chloride (feed)	40	0.1	4.14	1011
Sodium sulfate (solute)	2300	0.0018	4.14	588

mately 56. The concentration of the sodium sulfate (solute) inside the tank was set to 0.0018 M to give a molar ratio of 1:1. During each of the experiments, the concentration of solute inside the tank fell by 0.0018 M, which is stoichiometrically equivalent to the quantity or reactant feed, that is, 4.135 mols (see Table 1). Each of the two experiments used the Rushton disc turbine at a rotational speed of 75 rpm, which is comparable to industrial precipitation reactors.

The point at which the semi-batch feed is introduced into the vessel has a strong bearing on both the rate of mixing, and, therefore, reaction, as well as the observed mixing pattern. This will be of importance for systems where reaction rates are fast, which in turn may have an effect on both the crystal-size distribution (CSD), and observed crystal morphology. It is sensible to add any reactants at a point in the vessel where there are high levels of local flow and turbulence, which should aid the mixing process. For all experiments, the semi-batch feed was introduced midway between the impeller shaft and vessel wall.

The timewise conductivity profiles (equivalent conductivity changes) for the two semi-batch feed times $t_f = 7$ min and $t_f = 4$ min, are presented in Figure 6a and b. The upper line on the figure represents the 95th percentile of each frame of data, while the lower line represents the 5th percentile of each frame of data, that is, those pixels that have relatively high and low values, respectively. The midline on Figure 6a and b then represents the instantaneous average conductivity (for all pixels). The same three distinctive regions already described for a lab scale vessel can be clearly seen on the two profiles.

Although experiments conducted by Taguchi (1993)[22] were carried out on a small 150 mL vessel with higher concentrations of feed and different feed times, the general trend in conductivity is the same. That is, an increase in conductivity, at the start of the precipitation process (phase I), followed by distinctive maximum conductivity (period II), and a subsequent "tailing off" of the conductivity (period III). The rate at which the average conductivity value increases (linear in phase I), reduces even before the semibatch feed of barium chloride stops, which suggests changes in the reaction kinetics occurs before t_f. This could be as a result of an increase in the rate of solids formation due to the occurrence of a "critical" value of supersaturation for example. Like the result observed by Taguchi, in all sets of data the final conductivity is slightly higher than the starting conductivity.

The timewise conductivity profiles can be rescaled and plotted on the same axis to provide an indication of the influence of feed time on the semi-batch precipitation process (see Figure 7). For a feed time of 7 min, the peak conductivity is lower, and the conductivity profile tails off quite slowly. This is comparable to Figure 2, where the highest peak conductivity occurs at the lower feed rate, and the final conductivity level is slightly above the starting conductivity.

The presence of such a feed plume for times less than t_f is visualized in Figure 8. The images in the figure are generated from the raw ERT data. The equivalent color conductivity scale is also given in the figure. The first three, corresponding to times 1, 3 and 7 min, are 3-D triple iso-surface isometric representations of the vessel showing regions of high(est) conductivity. These regions of high(est) conductivity are undoubtedly due to the presence of dissociated barium and chloride ions, which are as yet unmixed and, therefore, unreacted. In fact, it is reasonable to assume that once the feed plume has been established most of the chemical reaction will take place on the periphery of this plume, where regions of supersaturation will exist for a short time before the primary nucleation takes place. The last two images, corresponding to times 10 and 14 min, are also generated from raw ERT data, but are represented as eight slices, each corresponding to one of eight ERT sensor planes. As expected, after the semi-batch feed has stopped (times greater than t_f) the feed plume is no longer observed. The conductivity during this period reduces (seen as a change in color).

Figure 9 highlights the conductivity distribution plots for each of the chosen times. These provide a strong indication of the departures from homogeneity within the vessel. The first three, each with a relatively wide distribution (less homoge-

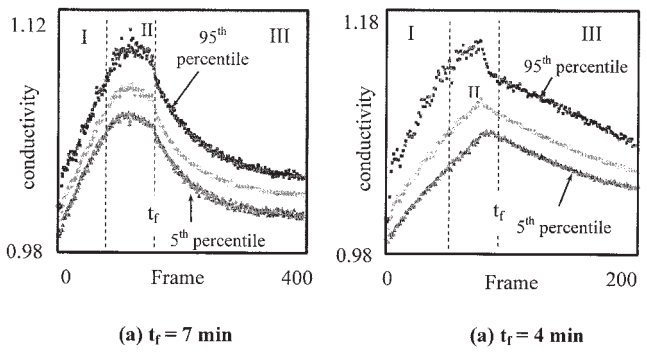

Figure 6. Conductivity variations per frame during the precipitation of $BaSO_4$, agitator at 75 rpm.

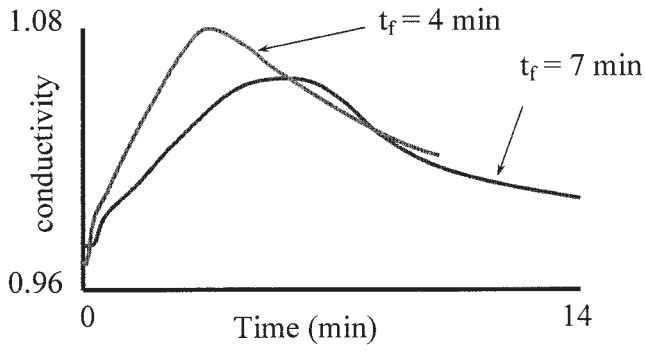

Figure 7. Profile of average pixel values for different feed times, t_f.

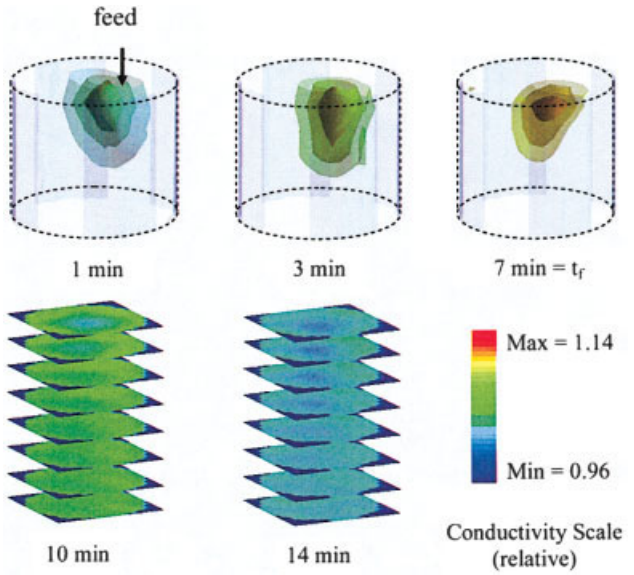

Figure 8. 3-D imaging of stirred vessel during precipitation of barium sulfate (t_f = 7 min).

neous), indicate the pixel distributions steady "migration" to the right (higher conducting) for times less than the feed time t_f. After the semi-batch feed ceases, the direction of this "migration" is reversed, and the pixel distribution moves back toward the left (lower conducting). The difference in the pixel distributions for 10 and 14 min is almost certainly due to secondary processes, such as crystal growth and/or Otswald ripening rather than a slow mixing process. It may be possible to infer kinetic information regarding the secondary process from the rate at which the conductivity reduces. Future planned work will utilize a "Lasentec" particle analyzer to track the crystal-size distribution as the reaction proceeds. This would provide a more comprehensive investigation into the formation and growth of crystals. The conductivity distributions for times of 10 and 14 min, both have a significantly narrower distribution (more homogeneous) than the previous three, that is, 1, 3 and 7 min. For 14 min, it is reasonable to assume that the reaction has in fact stopped, and any variations in conductivity could be due to variations in solid concentration. The data suggests that the solids distribution within the vessel for these

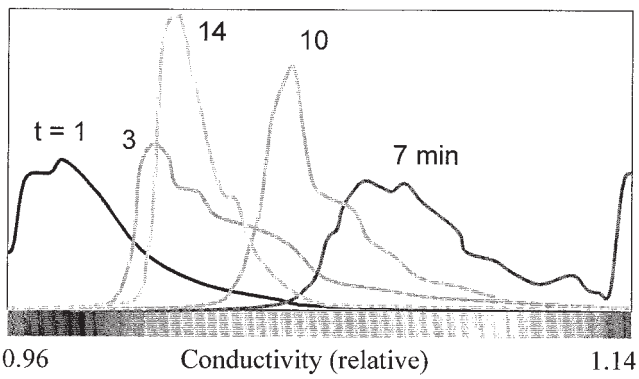

Figure 9. Pixel distribution plots during precipitation of barium sulfate (t_f = 7 min).

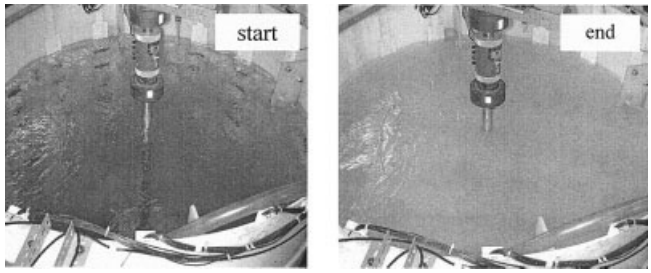

Figure 10. Photo images captured during the precipitation of $BaSO_4$, t_f = 7 min.

times is relatively homogeneous (that is, indicative of little solids settling out due to continuing mixing).

Because there was no obvious way to measure the quantity of $BaSO_4$ precipitate inside the vessel during the reaction, it was decided that digital images of the tank interior would be captured every minute for the duration of the experiment. $BaSO_4$ solid is a white precipitate that turns water cloudy, as seen in Figure 10. Clearly seen in the first image through the transparent water is the agitator, agitator shaft, baffles, and about half of the sensor sections. In the second image, taken at the end of the experiment, the fluid inside the vessel has become cloudy to the point of being totally opaque. To try and quantify the rate of solids formation, it was assumed that the amount of solids inside the vessel is related to the opacity of the mixture. The length of impeller shaft visible on each captured image was measured, and an equivalent "opacity function" was calculated (see Figure 11). The major increase in opacity/amount of precipitate for the mixture occurs in phase II, with relatively small increases occurring in phases I and II. This is comparable with the trend observed by Taguchi (1993)[19] who observed a similar significant rise in the measured magma density M_t, during phase II (see Figure 1). The photo images captured were used simply as an estimate as to when during the experiment the solids were formed.

Changed Conductivity Profiles Due to Impeller Failure

The two experiments reported above were repeated, but with the agitator switched off to investigate whether a similar,

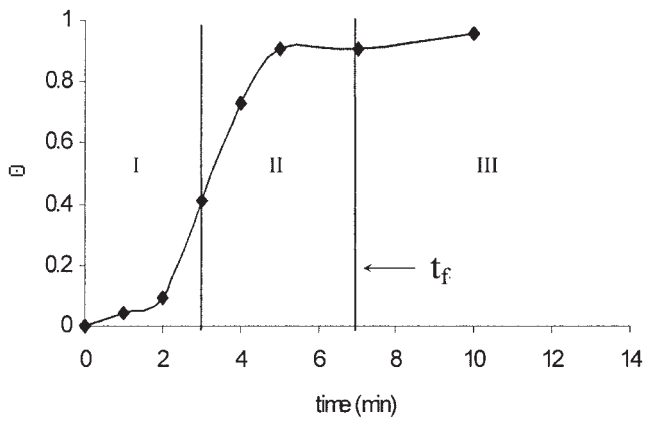

Figure 11. Opacity function of mixture inside vessel during barium sulfate precipitation.

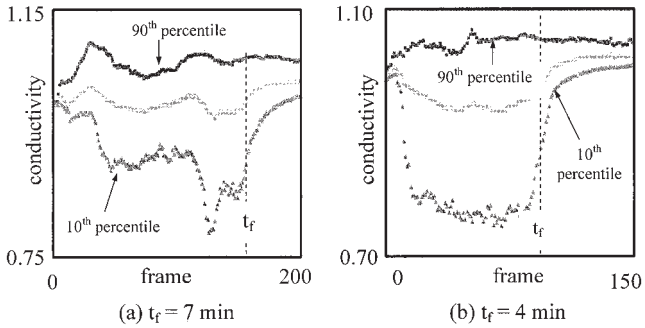

Figure 12. Conductivity profiles per frame for the precipitation reaction, agitator off.

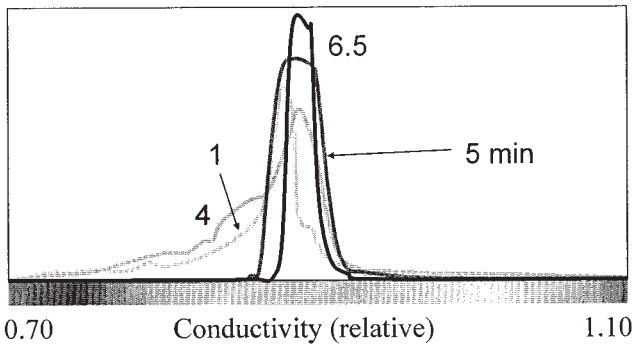

Figure 14. Pixel distribution plots during precipitation reaction, agitator off, (t_f =4min).

identical, or different conductivity profile would occur, and to look at the characteristics of any feed plume. The pixel values per frame (equivalent conductivity changes) for the two semi-batch feed times, t_f = 7 min and t_f = 4 min, are represented in Figure 12a and 12b. The upper line in the figures represents the 90th percentile, the lower line the 10th percentile, and the midline, the average pixel value. It is immediately obvious that the conductivity profiles are much different than the previous examples. There is no significant increase or decrease in the average measured conductivity, although there is a very slight increase in average conductivity at times greater that t_f.

Figure 13 shows the 3-D sliced images generated from the raw ERT data for a feed time t_f, of 4 min. The images in the figure represent times 1, 2, 4, 5 and 6.5 min after the semi-batch feed commences. Perhaps the most interesting deviation from the previous case (agitator on) is the nature of the feed plume during the semibatch feed addition stage. Previously, with the agitator on, the feed plume consisted of a higher conducting region (red), whereas with no agitation, the reverse is observed, that is, the feed plume consists of a lower conducting region (blue), which is clearly visible in the figure.

This could be due to the more intense formation of precipitate locally around the semibatch feed addition point. Because there is no agitation, the concentration of barium chloride around the semibatch feed addition point may build up to such a point that there may be an immediate formation of precipitate. The precipitation reaction would, therefore, consume the majority of ions in and around the feed point leaving an ion deficit, thus, seen as a low conducting "plume". Due to the lack of agitation, any barium chloride feed added after this will not

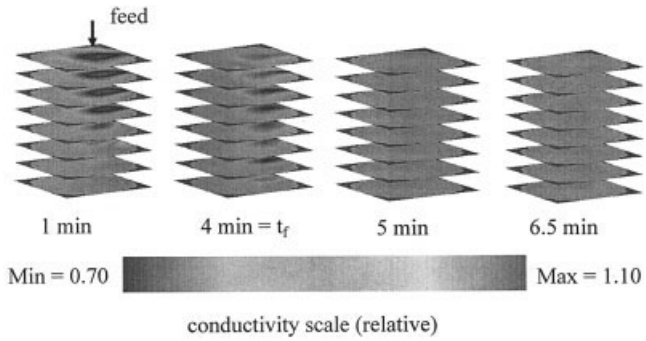

Figure 13. 3-D imaging during precipitation of barium sulfate, agitator off (t_f = 4 min).

come into contact with sodium sulfate for some time. Only the subtle convective mixing induced by the feed will transport the unreacted barium chloride into regions where sodium sulfate is present and available to form primary nucleates.

Figure 14 is the equivalent pixel distribution plots corresponding to the rendered images in Figure 13. As with the previous example (that is, agitator switched on), there is a definite "migration" toward a higher conductivity for times less than t_f, followed by a reverse "migration" toward a lower conductivity for times greater than t_f. For times less than t_f, the pixel distribution is relatively wide, suggesting low homogeneity inside the tank, although for times greater than t_f, the pixel distribution is significantly narrower (more homogeneous).

If the ERT system can detect different conductivity profiles and pathologies such as loss of agitation, then it follows that the ERT could be applied as a diagnostic tool in industry. As most reactors in industry tend to be sealed and are often pressurized, it would be advantageous to use an ERT system to detect any divergences from normal operational conditions, caused by mechanical failure of the agitator for example.

Interpretation of Conductivity Profiles

As we know, the ERT system predicts conductivity variations within the vessel, the interpretation of which can be a complex matter. There are numerous published mathematical techniques that attempt to correlate various important variables (such as supersaturation ratio and the degree of ionic dissociation) with conductivity measurements/values. These include the Debye-Huckel (Robinson and Stokes, 1959),[25] as well as the more recent mean spherical approximation method (Barthel *et al*, 2000),[26] which is more suited to noninfinite dilution electrolytes. When one attempts to apply such mathematical correlations it is of utmost importance that the distribution of dissociated ions and solid precipitate within the reactor are considered. Mathematical techniques of this type could be used to predict local concentrations of unmixed, dissociated (and therefore unreacted) ions induced by the departure from a perfectly mixed state, as well as spatial supersaturation ratios. Quantification of these spatial supersaturation ratios would be more suited to batch precipitation systems, where the reaction is controlled by temperature (slower precipitating systems). This technique may offer new possibilities for control action linked to spatio-temporal distributions of phases and compo-

nents for industrial applications, which may improve precipitate quality and aid the suppression of unwanted byproducts.

Conclusions

- A newly refurbished ERT system can produce up to around 2,500 data points inside the 3-D fluid space of a stirred precipitation reactor. Augmented reality images of fluid mixing processes have been created by solid-body iso-surface or sliced images that, with the use of color to denote conductivity, gives rise to a double-augmentation of the interior behavior producing a four or five dimensional format.
- An application to the precipitation of barium sulfate has been presented, which can readily highlight the different conductivity profiles within the vessel during the precipitation process for two different semibatch feed times. Three main regions have been highlighted during such a process reflecting the complex reaction and precipitation kinetics.
- The induced feed plume has been spatially quantified, via pixel distribution plots and 3-D images, to provide a powerful measure of the lack of homogeneity within a stirred vessel/reactor.
- This approach can also be used to highlight the different conductivity profiles and 3-D images obtained when the system is operating with no agitation, due to mechanical failure for example.
- It is believed this is the first application of ERT to a precipitation process.
- Further data interpretation regarding the quantification of spatial supersaturation ratios, as well as concentrations of dissociated ions in solution is possible.

Notation

a = Average diameter of ion, m
C_{Ba}^{2+} = Concentration of Barium ions, mol m^{-3}
C_{BaSO4}^{0} = Concentration of barium sulfate ion pairs, mol m^{-3}
I = Ionic strength, mol kg^{-1}
k_{sp}^{0} = thermodynamic solubility product, mol^2 kg^{-2}
M_t = Magma density, mol m^{-3}
S_a = Thermal supersaturation ratio
t_f = Feed time, s
V_{feed} = Volume of semibatch feed, m^3
V_{tank} = Volume of tank, m^3
Z_M, Z_A = Valence of ions M^{N+} and A^{M-}
γ_{BaSO4} = Mean activity coefficient of barium sulfate
Θ = Opacity function
κ = Reciprocal Debye - Huckel length, m

Acknowledgment

The authors gratefully acknowledge support from the EPSRC (Total Technology Studentship) and additional financial support from ITS (Industrial Tomography Systems), Manchester, UK.

Literature Cited

1. Söhnel O, Garside J. *Precipitation: Basic Principles and Industrial Application*. Oxford, U.K.: Butterworth-Heinemann, Ltd., 1992.
2. Williams RA, Beck MS. *Process Tomography: Principles, Techniques and Applications*. Oxford U.K.: Butterworth-Heinemann, Ltd., 1995.
3. Chaouki J, Lavachi F, Dudokovics MP. *Non-Invasive Monitoring of Multi-Phase Flows*. Amsterdam, Netherlands: Elsevier, 1997.
4. Yu ZZ, Peyton AJ, Beck MS, Conway WF, Xu LA. Imaging systems based on electromagnetic tomography (EMT). *Electronic Lett.*. 1993; 29(7).
5. Dyakowski T, Wang SJ, Geldart D, Beck MS. Tomographic studies of flow patterns within a circulating fluidised bed. *Chem. Eng. Comm*. 1999;175:117-130.
6. Mann R, Dickin FJ, Wang M, Dyakowski T, Williams RA, Edwards RB, Forrest AE. Application of electrical resistance tomography to interrogate mixing processes at plant scale. *Chem. Eng. Sci*. 1997; 52(13):2087-2097.
7. Stanley SJ, Wabo E, Mann R, Primrose K. Dual-validation of miscible liquid mixing in a stirred vessel imaged by electrical resistance tomography. 2nd World Congress Process Tomography. Hannover, Germany. 2001:151-158.
8. Wang M, Dorwood A, Vlaev D, Mann R. Measurements of gas-liquid mixing in a stirred vessel using electrical resistance tomography. *Chem. Eng. Sci.* 2000;77:93-98.
9. Holden PJ, Mann R, Wang M, Dickin FJ, Edwards RB. Imaging stirred-vessel macromixing using electrical resistance tomography. *AIChE J.*. 1998, 44(4):780-790.
10. Holden PJ, Wang M, Mann R, Dickin FJ, Edwards RB. On detecting mixing pathologies inside a stirred vessel using electrical resistance tomography (ERT). *Trans IChemE.* 1999;77(A):709-712.
11. Sahu AK, Kumar P, Patwardhan AW, Joshi JB. CFD modelling and mixing in stirred tanks. *Chem. Eng. Sci.* 1999;54:2285-2293.
12. Brucato A, Ciofalo M, Grisafi F, Tocco R. On the simulation of stirred tank reactors via computational fluid dynamics. *Chem. Eng. Sci.* 2000; 55:291-302.
13. Micale G, Montante G, Grisafi F, Brucato A, Godfrey J. CFD simulation of particle distribution in stirred vessels. *Trans IChemE.* 2000; 78(A):435-434.
14. Zauner R, Jones AG. Mixing effects on product particle characteristics from semi-batch crystal precipitation. *Trans IChemE*. 2000;78:894-901.
15. Mann R, Stanley SJ, Vlaev D, Wabo E, Primrose K. Augmented-reality visualisation of fluid mixing in stirred chemical reactors using electrical resistance tomography (ERT). J.*of Electronic Imaging*. 2001; 10(3):620-629.
16. Stanley SJ, Mann R, Primrose K. Tomographic imaging of fluid mixing in 3-D for single-feed semi-batch operation of a stirred vessel. *Trans. IChemE*, 2002;80(A):903-909.
17. Stanley SJ, Hristov H, Mann R, Primrose K. On reconciling tomographic measurements with a fluid mixing model for semi-batch operation of a stirred vessel. Proc: 3rd World Congress Process Tomography. Banff, Canada. 2003:834-839.
18. Rahimi M, Mann R. Macro-mixing, partial segregation and 3-D selectivity fields inside a stirred reactor. *Chem. Eng. Sci*. 2001;56:763-769.
19. Hristov H. Network-of-zones model for a bioreactor with a novel impeller. PhD Thesis. 2003: UMIST, UK.
20. Aoun M, Plasarri E, David R, Villermaux J. A simultaneous determination of nucleation and growth rates from batch spontaneous precipitation. *Chem. Eng. Sci*. 1999;54(9):1161-1180.
21. Phillips R, Rohani S, Baldyga J. Micromixing in a single-feed semi-batch precipitation process. *AIChE J*. 1999;45(1):82-92.
22. Taguchi K. Precipitation of barium sulfate: kinetics of nucleation and growth and the influence of mixing. PhD Thesis. 1993: UMIST, UK.
23. ITS P2000 Users Manual: Industrial Tomography Systems, Manchester, UK. www.itoms.com.
24. Wang M. Inverse solutions for electrical impedance tomography based on conjugate gradients methods. *Meas. Sci. Technol*. 2002;13:101-117.
25. Robinson RA, Stokes RH. Electrolyte Solutions, London, UK: Butterworths, 1959.
26. Barthel J, Krienke H, Holovko MF, Kapko VI, Protsykevich IA. The application of the associative mean spherical approximation in the theory of non aqueous electrolyte solutions. *Condensed Matter Physics*, 2000;3(23):657-674.

Manuscript received Feb. 25, 2004, and revision received June 23, 2004.